Acknowledgments

This work was supported by EPRI Contract No. RP8001-4. The authors would like to thank F. Goodman of EPRI and G. Fiegl of UniSil for the helpful discussions and the growth of MCZ samples.

Manuscript submitted July 23, 1990; revised manuscript received Sept. 26, 1990.

Georgia Institute of Technology assisted in meeting the publication costs of this article.

REFERENCES

1. I. Yonenaga, K. Sumino, and K. Hoshi, *J. Appl. Phys.*, **56,** 2346 (1984).
2. K. Hoshi, N. Isawa, T. Suzuki, and Y. Ohkubo, *This Journal*, **132,** 693 (1985).
3. A. Hara, T. Fukuda, T. Miyabo, and I. Hirai, *J. Appl. Phys.*, **66,** 3958 (1989).
4. W. Lin and A. S. Oates, *Appl. Phys. Lett.*, **56,** 128 (1990).
5. K. Sumino, H. Harada, and I. Yonenaga, *Jpn. J. Appl. Phys.*, **19,** L49 (1980).
6. K. H. Yang, H. F. Kappert, and G. H. Schwuttke, *Phys. Status Solidi (A)*, **50,** 221 (1978).
7. S. Kishino, M. Kanamori, N. Yoshihiro, M. Tajima, and T. Lizuka, *J. Appl. Phys.*, **50,** 8240 (1979).
8. R. A. Sinton, Y. Kwark, J. Y. Gan, and R. M. Swanson, *IEEE Electron Device Lett.*, **EDL-7,** 567 (1986).
9. A. W. Blakers, A. Wang, A. M. Milne, J. Zhao, and M. A. Green, *Appl. Phys. Lett.*, **55,** 1363 (1989).
10. S. Kawado, T. Maruyama, T. Suzuki, N. Isawa, and K. Hoshi, *This Journal*, **133,** 171 (1986).
11. T. Higuchi, E. Gaylord, G. A. Rozgonyi, and F. Shimura, *Appl. Phys. Lett.*, **53,** 1850 (1988).
12. S. K. Pang and A. Rohatgi, 19th IEEE Photovoltaic Specialists Conference, pp. 1500-1501, New Orleans, LA, May 4-8, 1987.
13. Annual Book of ASTM Standards, F121 and F123, American Society of Testing and Materials, Philadelphia, PA (1984).
14. E. Yablonovitch, D. L. Allara, C. C. Chang, T. Gmitter, and T. B. Bright, *Phys. Rev. Lett.*, **57,** 249 (1986).
15. W. Shockley and W. T. Read, *Phys. Rev.*, **87,** 835 (1952).
16. R. N. Hall, *ibid.*, **87,** 387 (1952).
17. P. T. Landsberg, *Appl. Phys. Lett.*, **50,** 745 (1987).
18. S. K. Pang, A. Rohatgi, B. L. Sopori, and G. Fiegl, *This Journal*, **137,** 1977 (1990).
19. A. Ohsawa, K. Honda, and N. Toyokura, *ibid.*, **131,** 2964 (1984).
20. M. Futagami, K. Hoshi, N. Isawa, T. Suzuki, Y. Kato, and Y. Okamoto, in "Semiconductor Silicon 1986," H. R. Huff, T. Abe, and B. Kolbesen, Editors, PV 86-4, p. 939, The Electrochemical Society Softbound Proceedings Series, Pennington, NJ (1986).
21. M. Hourai, T. Naridomi, Y. Oka, K. Murakami, S. Sumita, N. Fujino, and T. Shiraiwa, *Jpn. J. Appl. Phys.*, **27,** L2361 (1988).
22. M. Hourai, K. Murakami, T. Shigematsu, N. Fujino, and T. Shiraiwa, *ibid.*, **28,** 2413 (1989).
23. Q. Sun, K. H. Yao, J. Lagowski, and H. C. Gatos, *J. Appl. Phys.*, **67,** 4313 (1990).
24. R. Nagasawa, Y. Matsushita, and S. Kishino, *Appl. Phys. Lett.*, **37,** 622 (1980).

Forced and Natural Convection Effects on the Shape Evolution of Cavities during Wet Chemical Etching

Chee Burm Shin* and Demetre J. Economou**

Department of Chemical Engineering, University of Houston, Houston, Texas 77204-4792

ABSTRACT

The effect of forced and natural convection on the shape evolution of deep cavities during wet chemical etching was investigated. Etching was assumed to be limited by removal of the dissolution products away from the vicinity of the active surface. Finite element methods were employed to solve for the fluid velocity and product concentration distributions in cavities of irregular geometries resulting from etching. Forced convection was found very ineffective for rinsing deep cavities. The etching rate decreased sharply with time as the cavity became deeper during etching. At the same time, the etching rate distribution along the active surface became nearly uniform, degrading etch anisotropy. In contrast, natural convection was effective for rinsing the dissolution products out of the cavity. Both the etching rate and the etch factor remained at relatively high values throughout etching, even at later times when the cavity became deeper. The cavity wall profiles and the corresponding flow and concentration fields showed some interesting features, especially for the case of natural convection. The results have important implications for deep anisotropic etching and other related processes.

Wet chemical etching is widely employed in the electronics industry for etching thin and thick films (a few microns to hundreds of microns thick). The method is characterized by high etching rate and excellent selectivity (1). Examples include etching of compound semiconductors for the fabrication of optoelectronic devices (2, 3) and etching of copper films for the fabrication of printed circuit boards (4). When etching is dominated by crystallographic effects, features of extremely high aspect ratio (depth: width) can be obtained without mask undercut (5). In the absence of crystallographic effects, however, significant mask undercut may result. In the following, emphasis will be placed on systems for which crystallographic effects are not important. The case of crystallographic etching may be analyzed based on knowledge of the reaction kinetics and geometric considerations alone (6).

Important goals of the etching process are high etching rate and minimum mask undercut. When etching is limited by surface reaction kinetics, the etching rate is relatively low and the mask undercut equals the etched depth (etch factor equal to unity). The situation can be improved when the system is operated under mass-transfer control. Under such conditions the mass-transfer rate, and therefore the etching rate, may be increased by the effect of fluid flow over the reacting surface. Examples include forced convection by impinging jet or shear flow past the surface (7, 8). When etching is influenced by mass transfer, the shape of the topographical feature, or cavity, depends in a complicated manner on the hydrodynamic conditions prevailing in the cavity region, since such conditions influence the mass-transfer rate. The etching rate distribution along the cavity walls depends on the instantaneous shape of the cavity, which in turn affects the further shape evolution of the cavity. Fluid flow by forced convection is effective for enhancing mass transport at the initial stages of etching when the cavity is still shallow and the flow can penetrate the cavity. However, as the cavity deepens during etching, slow recirculating eddies form within the cavity, preventing effective communication between the external flow and that inside the cavity. The result is a drastic decrease in the etching rate and degradation of etch anisot-

* Electrochemical Society Student Member.
** Electrochemical Society Active Member.

ropy (low etch factor). It appears that deep anisotropic etching is not possible by forced convection alone.

Recently, remarkable advances have been made in achieving deep anisotropic etching which does not depend on the crystallographic orientation of the film. Thus, Podlesnik *et al.* (9) used laser-assisted techniques to etch extremely deep submicron features with aspect ratio of the order of 100:1. However, as the authors pointed out, important questions pertaining to density-gradient induced flows and mass transfer within the cavity remain unanswered. A unique method to enhance mass transfer in deep cavities makes use of such density-gradient induced flows (10). Kuiken and Tijburg used natural convection, enhanced by using an artificial gravity environment, to achieve high-rate anisotropic etching.

The effect of fluid flow on the mass transfer in cavities of fixed shape has been studied extensively. Alkire and coworkers (8, 11) studied the effectiveness of forced convection in removing the dissolution products away from the cavity interior. Kuiken (12) presented a mathematical analysis of heat and mass transfer in cavities under the influence of forced convective flow. Mass transfer in open cavities under the influence of natural convection has received much less attention. This may be due to the complex interaction between internal flows and external conditions. Shin and Economou (13) presented a numerical simulation of transient mass transfer in cavities of fixed shape under the influence of natural convection. The effect of cavity aspect ratio and of Rayleigh number was studied.

Despite the importance of the problem, studies of the shape evolution of cavities are scarce. Vuik and Cuvelier (14) studied the effect of diffusion and reaction on the shape evolution of two-dimensional cavities in the absence of fluid flow (pure diffusion). Kuiken (15-17) presented semianalytical solutions of the etching profiles of cavities in the absence of fluid flow and under mass-transfer control. Shin and Economou (18), investigated the effect of forced convection on the shape evolution of two-dimensional cavities. Finite element methods were employed to solve for the fluid velocity and concentration fields in cavities of irregular shape resulting from etching. A moving boundary scheme was developed to track the shape evolution of the cavity. The instantaneous etching rate distribution along the cavity walls was computed as a function of time. The effect of fluid flow on the etching rate was reduced as the cavity became deeper and an eddy formed which prevented effective communication between the external flow and the interior of the cavity. Results in terms of cumulative etch rate and etch factor were compared to the case of pure diffusion.

The present investigation is an extension of the previous study (18). The effect of forced convection on the shape evolution of cavities was studied for higher values of the Peclet number (up to 10^4). In addition, the effect of natural convection was investigated for values of the Rayleigh number of up to 10^4. Although chemical etching is being emphasized, the results of this study are not limited to the etching problem but may be applied to, for example, electrodeposition through masks (19), or localized corrosion (11), or other natural and forced convection problems conforming to the system configuration and to the model assumptions.

Mathematical Formulation

Natural convection system.—A schematic of the natural convection system is shown in Fig. 1. A solid film is partially protected by a resist mask having thickness h. Initially, the mask forms a rectangular cavity of width $2L$ in the unprotected area of the film [film surface at position $\Gamma_1(0)$]. The third dimension (along z) of the cavity was assumed long, and therefore a two-dimensional system was considered. The etching solution reacts selectively with the exposed film without attacking the resist mask. Etching takes place under the influence of an acceleration field as shown in Fig. 1. The film dissolution products enter the solution altering the local solution density. The density gradients induce convective flow patterns which affect the rate of mass transport to and from the reactive surface. The etching rate distribution along the active walls of the cavity depends on the instantaneous shape of the cavity, which in turn affects the further shape evolution of the cavity. During etching, the outer boundary Γ_∞ remains fixed in time. However, boundaries $\Gamma_1(t)$ and $\Gamma_2(t)$ evolve with time. (Boundary Γ_2 includes the mask portion in the undercut region; since the mask undercut evolves with time, boundary Γ_2 is time dependent as well.)

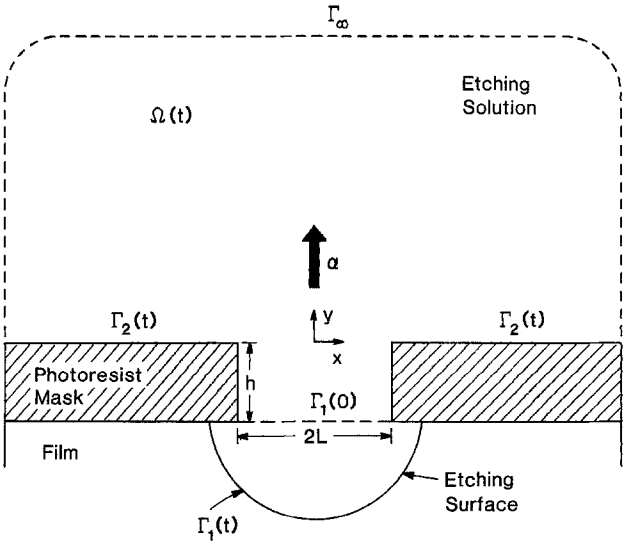

Fig. 1. Schematic of the natural convection system. The acceleration field α is applied in the y direction.

The following assumptions were introduced in order to streamline the computational task. (*i*) The film dissolution rate was assumed to be controlled by the mass transport of reaction products away from the surface. Hence, at all times, the product concentration on the film surface $\Gamma_1(t)$ was taken equal to the product saturation concentration in the etching solution. (*ii*) The fluid was assumed incompressible and Newtonian, and the system was assumed isothermal with constant physical properties except for the solution density. (*iii*) The usual Boussinesq approximation was applied, assuming a constant density in all terms except the body-force term of the Navier-Stokes equations. (*iv*) The solution density was assumed to depend on the concentration of the reaction product according to the following equation of state

$$\rho = \rho_\infty[1 + \beta(c - c_\infty)] \qquad [1]$$

Under the above assumptions the governing equations are written as

$$\frac{\partial \mathbf{u}}{\partial t} + \mathbf{u} \cdot \nabla \mathbf{u} = -\frac{1}{\rho_\infty} \nabla p + \nu \nabla^2 \mathbf{u} + \frac{\rho}{\rho_\infty} \alpha \quad \text{in } \Omega(t) \qquad [2]$$

$$\nabla \cdot \mathbf{u} = 0 \quad \text{in } \Omega(t) \qquad [3]$$

$$\frac{\partial c}{\partial t} + \mathbf{u} \cdot \nabla c = D \nabla^2 c \quad \text{in } \Omega(t) \qquad [4]$$

Equation [2] is the Navier-Stokes equation for the fluid velocity field. Equation [3] is the continuity equation for the incompressible fluid, and Eq. [4] is the convective-diffusion equation for the concentration distribution of the reaction product.

The governing equations were rendered dimensionless by defining

$$(X, Y) = \frac{1}{L}(x, y) \qquad T = \frac{tD}{L^2} \qquad [5]$$

$$\mathbf{U} = \frac{L}{D}\mathbf{u} \qquad P = \frac{(p - \rho_\infty \alpha y)L^2}{\mu D} \qquad [6]$$

$$C = \frac{c - c_\infty}{c_{sat} - c_\infty} \quad [7]$$

$$Sc = \frac{\nu}{D} \qquad Ra = \frac{\alpha\beta(c_{sat} - c_\infty)L^3}{D\nu} \quad [8]$$

The cavity half-width L was used as the characteristic length to define the Rayleigh number, although the cavity depth may be a more appropriate scale. However, in the present situation, the cavity depth is a time-varying quantity, and it is not convenient for defining Ra.

The dimensionless form of the governing equations is

$$\frac{1}{Sc}\left(\frac{\partial \mathbf{U}}{\partial T} + \mathbf{U}\cdot\nabla\mathbf{U}\right) = -\nabla P + \nabla^2\mathbf{U} + Ra\,C\mathbf{j} \quad \text{in } \Omega(T) \quad [9]$$

$$\nabla\cdot\mathbf{U} = 0 \quad \text{in } \Omega(T) \quad [10]$$

$$\frac{\partial C}{\partial T} + \mathbf{U}\cdot\nabla C = \nabla^2 C \quad \text{in } \Omega(T) \quad [11]$$

Equations [9]-[11] are coupled through the dependence of the solution density on the product concentration (see Eq. [1]) which appears in the last term in Eq. [9]. The degree of coupling depends on the value of Ra. The higher the value of Ra, the stronger the coupling between the flow and concentration fields.

The corresponding boundary and initial conditions are

$$\frac{\partial \mathbf{U}}{\partial n} = 0 \qquad C = 0 \quad \text{on} \quad \Gamma_\infty \quad [12]$$

$$\mathbf{U} = 0 \qquad \frac{\partial C}{\partial n} = 0 \quad \text{on} \quad \Gamma_2(T) \quad [13]$$

$$\mathbf{U} = 0 \qquad C = 1 \quad \text{on} \quad \Gamma_1(T) \quad [14]$$

$$\mathbf{U} = 0 \qquad C = 0 \quad \text{in } \Omega \quad \text{at } T = 0 \quad [15]$$

where $\partial/\partial n$ denotes the gradient in the outward direction normal to the boundary.

Boundary condition Eq. [12] implies that the product concentration far from the reacting surface remains equal to c_∞. Boundary condition Eq. [13] implies that the product does not react with or penetrate into the mask.

The movement of the boundary was described by

$$v_n = -\sigma\nabla c\cdot\mathbf{n} \quad [16]$$

which in dimensionless form became

$$V_n = -\frac{1}{B}\nabla C\cdot\mathbf{n} \quad [17]$$

Parameters σ and B are given by

$$\sigma = \frac{DM_s}{\rho_s} \qquad B = \frac{D}{\sigma(c_{sat} - c_\infty)} \quad [18]$$

Parameter B gives a measure of the speed of the boundary movement. When B is very large, the boundary moves only very slowly. Under this condition, the species concentration profiles can relax on a time scale much faster than the boundary movement.

The parameters of the problem are the Schmidt number, Sc, the Rayleigh number, Ra, the initial cavity aspect ratio, $A(= h/2L)$, and the value of B. The problem is to compute the time-dependent location of boundary $\Gamma_1(t)$ for specified values of the above parameters. The etching rate and etch factor can then be determined.

For the problem at hand, the etching rate is proportional to the mass-transfer rate (Eq. [17]). The dimensionless local mass-transfer rate was expressed as a local Sherwood number

$$Sh_x = \frac{k_x L}{D} = \frac{\partial C}{\partial n} \quad [19]$$

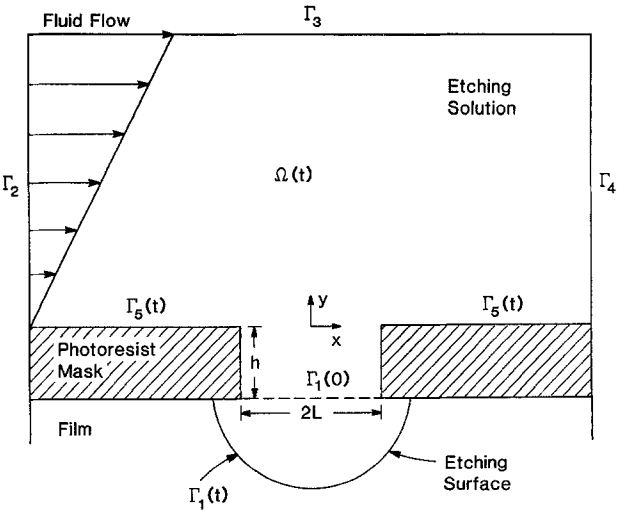

Fig. 2. Schematic of the forced convection system. A simple shear flow prevails far from the cavity.

The limiting case of pure diffusion (no fluid flow) was obtained by setting Ra = 0 in Eq. [9], which, for the initial and boundary conditions given by Eq. [12]-[15], resulted in $\mathbf{U} = \mathbf{0}$ at all times.

Forced convection system.—The forced convection system is shown in Fig. 2. The system is similar to that of Fig. 1 except that the acceleration field is absent, and that a shear flow prevails far from the cavity. The following assumptions were made for this system. (*i*) The film dissolution rate was assumed to be controlled by the mass transport of reaction products away from the surface. Hence, at all times, the product concentration on the film surface $\Gamma_1(t)$ was taken equal to the product saturation in the etching solution. (*ii*) The fluid was assumed incompressible and Newtonian, and the system was assumed isothermal with constant physical properties (including the solution density). In the forced convection system, boundaries Γ_2, Γ_3, and Γ_4 are fixed in time. However, boundaries $\Gamma_1(t)$ and $\Gamma_5(t)$ are evolving with time. The initial location of the moving boundary is at $\Gamma_1(0)$.

The same governing equations apply as before (Eq. [9]-[11]) with Ra = 0. The boundary and initial conditions appropriate for the forced convection system are (8, 18)

$$\mathbf{U} = \mathbf{0} \qquad C = 1 \quad \text{on} \quad \Gamma_1(T) \quad [20]$$

$$U_x = \Sigma Y \qquad U_y = 0 \qquad C = 0 \quad \text{on} \quad \Gamma_2 \quad [21]$$

$$U_x = \text{constant} \qquad U_y = 0 \qquad \frac{\partial C}{\partial n} = 0 \quad \text{on} \quad \Gamma_3 \quad [22]$$

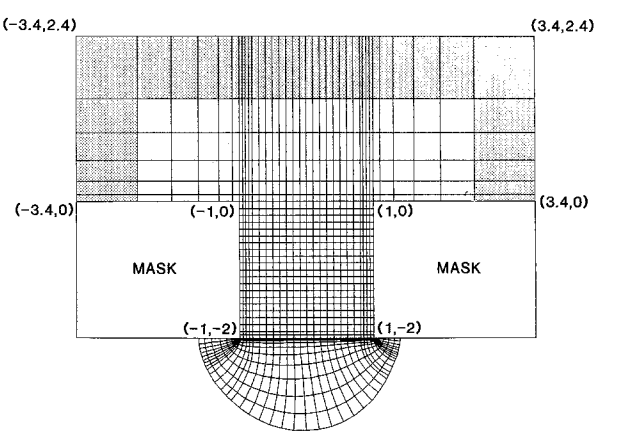

Fig. 3. A representative finite element mesh used for the natural convection system. The dotted elements are mapped infinite elements; the rest are normal finite elements.

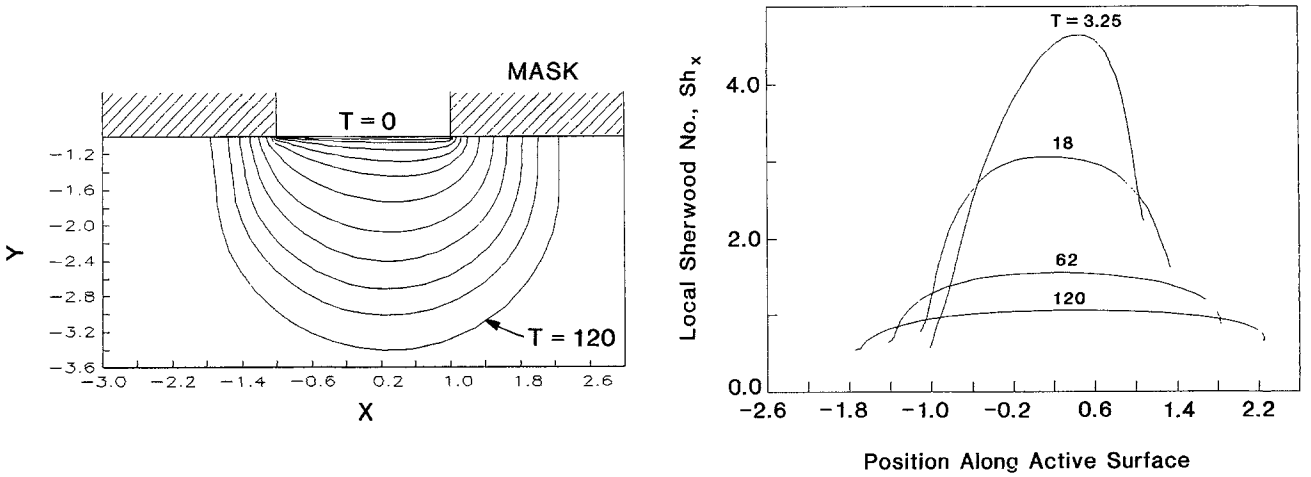

Fig. 4. (a, left) Shape evolution of a cavity with initial aspect ratio of 1:2 under forced convection. Other conditions were Pe = 10^3, Re = 1, and B = 100. Cavity wall profiles are shown for dimensionless times T = 0, 0.7, 1.5, 3.25, 6, 10, 18, 30, 44, 62, 84, and 120. (b, right) Local Sherwood number (instantaneous etching rate) distribution along the active surface at different times during etching. Conditions were as in (a).

$$\frac{\partial U_x}{\partial n} = U_y = 0 \qquad \frac{\partial C}{\partial n} = 0 \quad \text{on} \quad \Gamma_4 \qquad [23]$$

$$\mathbf{U} = 0 \qquad \frac{\partial C}{\partial n} = 0 \quad \text{on} \quad \Gamma_5(T) \qquad [24]$$

$$\mathbf{U} = \mathbf{U}_0 \qquad C = 0 \quad \text{in} \quad \Omega \quad \text{at} \quad T = 0 \qquad [25]$$

Here $\mathbf{U}_0$ is the velocity field obtained when the moving boundary is at position $\Gamma_1(0)$. The movement of the boundary was described by Eq. [17]. In the forced convection system the relevant parameters are the initial cavity aspect ratio A, the Reynolds number defined by Eq. [26] below, the Peclet number Pe = Re Sc, and parameter B

$$\text{Re} = \frac{u_c L}{\nu} \qquad [26]$$

In contrast to the analysis presented in Ref. (18), the Reynolds and Peclet numbers do not appear explicitly in the governing Eq. [9]-[11] due to the different scaling used for velocity (see Eq. [6]). However Re is directly related to the applied shear rate Σ (Eq. [21]), and therefore to the value of U_x on boundary Γ_3 (Eq. [22]). Again, the problem is to find the location of the moving boundary $\Gamma_1(t)$ as a function of time during etching. The etching rate and etch factor can then be computed for a given set of parameter values.

Method of Solution

Natural convection system.—The solution to the governing Eq. [9]-[11] subject to the associated boundary conditions [12]-[15] was obtained by using the finite element method. A typical finite element mesh is shown in Fig. 3. This mesh corresponds to the cavity of Fig. 9a below at time T = 148. The mesh was made finer around the mouth of the cavity and within the cavity where steeper concentration gradients are expected. Because the physical domain is unbounded, a problem arises regarding the size of the computational domain, more specifically the location of boundary Γ_∞. Various methods have been proposed to overcome the difficulty associated with an unbounded domain (20-22). One approach is to position Γ_∞ far from the cavity mouth, so that conditions near the cavity are not affected by the exact location of the boundary. This approach may result in unnecessarily large computational domain and hence more CPU time to obtain the solution. Another method was adopted in this work, namely, the "mapped infinite element" method (23, 24). This method is particularly attractive when used in combination with conventional elements. The elements of the outermost layer in Fig. 3 (dotted area) were mapped infinite elements. The rest were conventional bilinear quadrilateral elements. The total number of elements and nodal points used for the mesh in Fig. 3 are 1186 and 1269, respectively. The total number of elements increased with time as the cavity became deeper during etching. Preliminary computer experiments showed that further refinement of the mesh had no

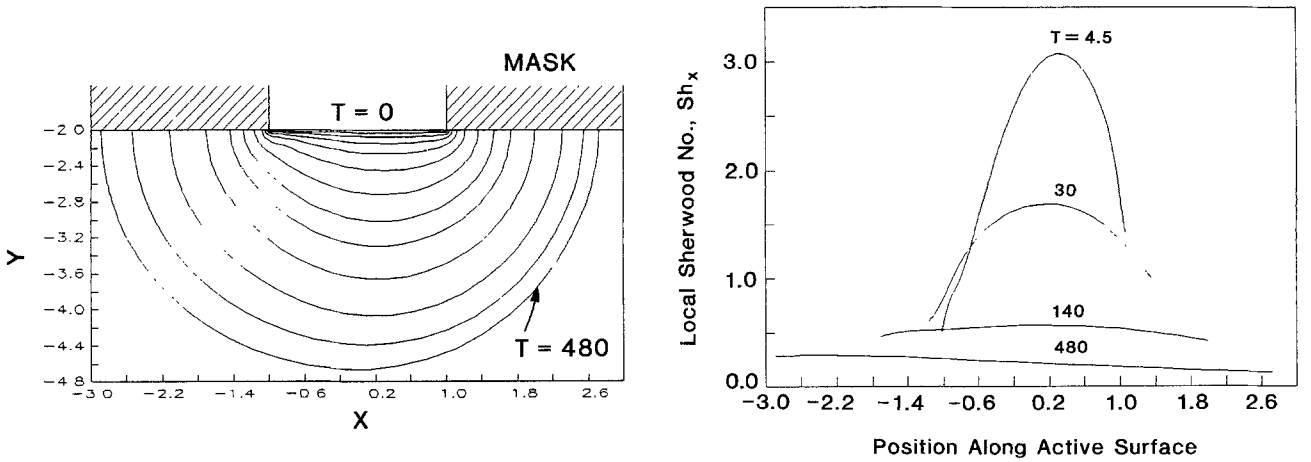

Fig. 5. (a, left) Shape evolution of a cavity with initial aspect ratio of 1:1 under forced convection. Other conditions were Pe = 10^3, Re = 1, and B = 100. Cavity wall profiles are shown for dimensionless times T = 0, 0.95, 2.25, 4.5, 8.5, 16, 30, 52, 82, 140, 240, 360, and 480. (b, right) Local Sherwood number (instantaneous etching rate) distribution along the active surface at different times during etching. Conditions were as in (a). The shear rate Σ (Eq. [21]) for the initial cavity is 3.418 × 10^3.

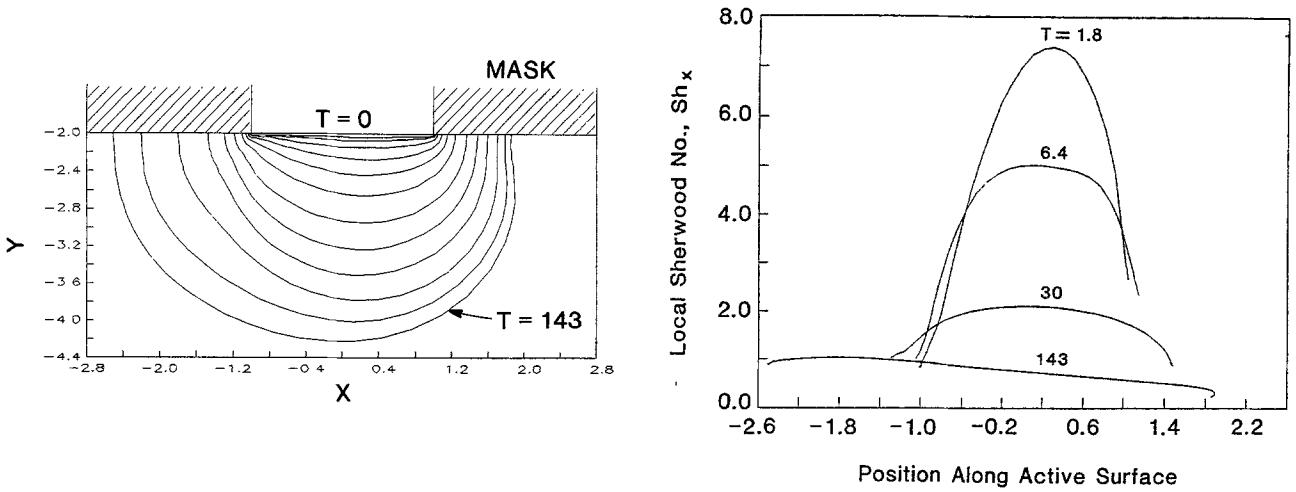

Fig. 6. (a, left) Shape evolution of a cavity with initial aspect ratio of 1:1 under forced convection. Other conditions were Pe = 10^4, Re = 10, and B = 100. Cavity wall profiles are shown for dimensionless times T = 0, 0.44, 0.84, 1.8, 3.6, 6.4, 11, 19, 30, 47, 76, 112, and 143. (b, right) Local Sherwood number (instantaneous etching rate) distribution along the active surface at different times during etching. Conditions were as in (a). The shear rate Σ (Eq. [21]) for the initial cavity is 3.581 × 10^4.

appreciable effect on the results for the parameter range investigated.

The velocity and concentration fields in the computational domain were obtained by using the penalty function formulation and the streamline upwind/Petrov Galerkin (SU/PG) finite element method (25, 26). Time integration was performed using an implicit predictor-multicorrector scheme (27) with variable time step. A fixed time step may be used as long as stability is assured. However, the fixed time step method may not be as cost effect. For example, a small time step may be required to accurately track the transient behavior of the system during a particular time period, whereas a much larger time step may be adequate for a different time period. In such cases, a variable time step is more effective. The variable time step algorithm used in the present work is similar to Bailey's method (28).

The transient solution to the two-dimensional problem was obtained in a sequential manner by decoupling the velocity and concentration fields (29, 30). At time T^n, the velocity field $\mathbf{U}^n$ and the concentration field C^n were known. Here superscript n denotes the nth time step and $T^0 = 0$. Then $\mathbf{U}^{n+1}$ and C^{n+1} were obtained through the following substeps:

1. With C^n known, $\mathbf{U}^{n+1}$ was calculated from Eq. [9] and [10] and the associated boundary conditions with an implicit predictor-multicorrector algorithm. If more than five iterations were needed in the corrector step to obtain $\mathbf{U}^{n+1}$, the time step was halved and calculations returned to the predictor step.
2. With $\mathbf{U}^{n+1}$ known from substep 1 above, C^{n+1} was calculated from Eq. [11] and the associated boundary conditions with an implicit predictor-multicorrector algorithm.

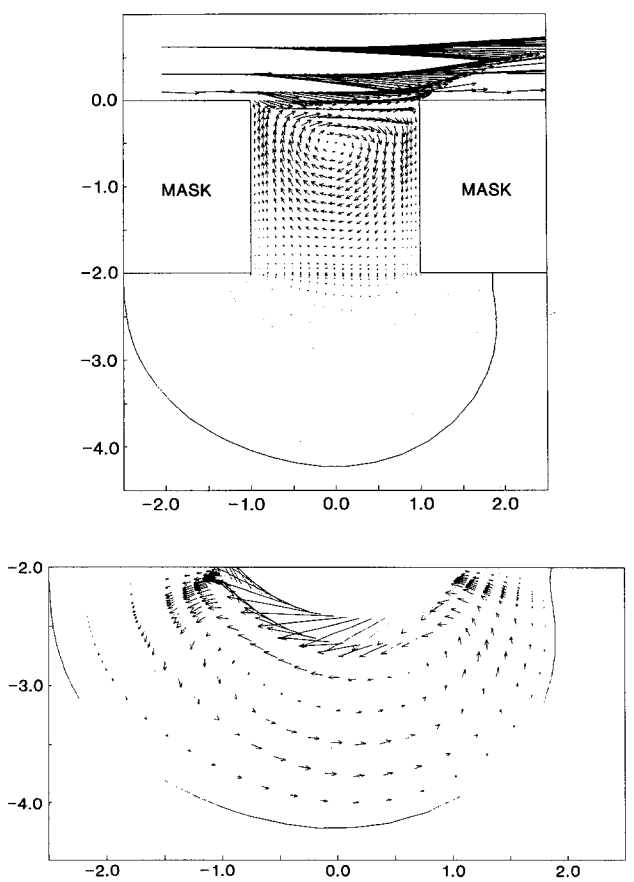

Fig. 7. (a, top) Velocity vector plot in the cavity corresponding to time T = 143 of Fig. 6. Velocity scale is 1.1 × 10^4. (b, bottom) Expanded scale of velocity vector plot in the lower part of the cavity in (a). Velocity scale is 1.1 × 10^2.

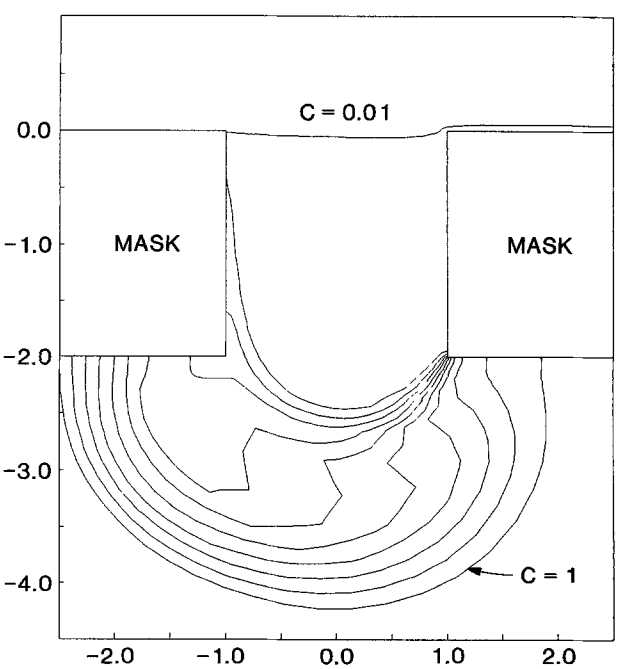

Fig. 8. Concentration contour plot in the cavity corresponding to T = 143 of Fig. 6. Linear interpolation applies for the contours between C = 0.01 and C = 1 (wall of cavity).

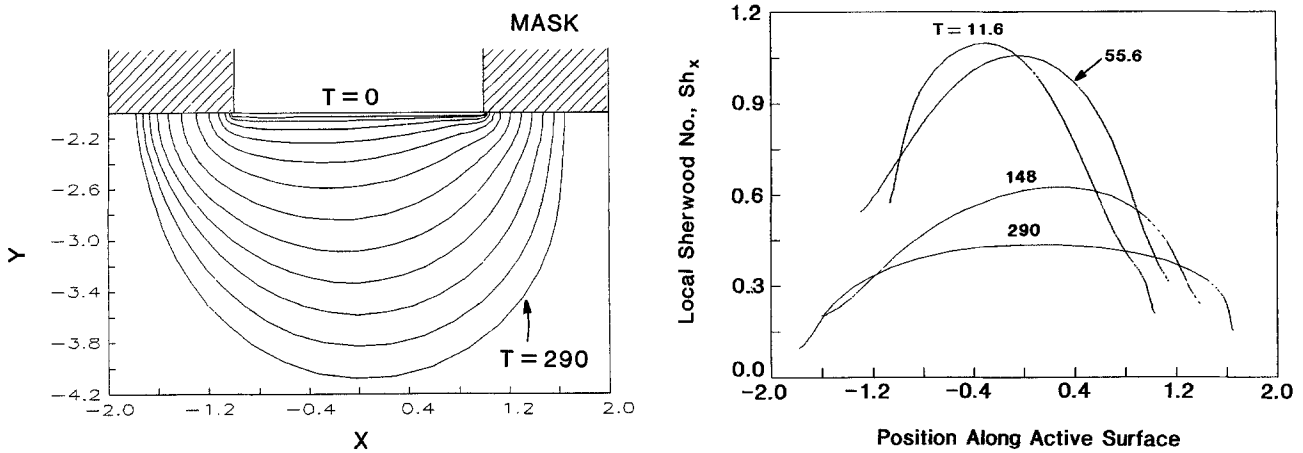

Fig. 9. (a, left) Shape evolution of a cavity with initial aspect ratio of 1:1 under natural convection. Other conditions were Ra = 10^3 and B = 100. Cavity wall profiles are shown for dimensionless times T = 0, 3.16, 5.96, 11.6, 21.6, 35.5, 55.6, 83.6, 114, 148, 188, 236, and 290. (b, right) Local Sherwood number (instantaneous etching rate) distribution along the active surface at different times during etching. Conditions were as in (a).

3. The Euclidean norm V^{n+1} of $\mathbf{U}^{n+1}$, and in turn the quantity ϵ was calculated by

$$\epsilon = \frac{|V^{n+1} - V^n|}{V^{n+1}} \qquad [27]$$

If $\epsilon < 0.01$, the time step was doubled. If $\epsilon > 0.1$, the time step was halved. If $0.01 < \epsilon < 0.1$ the time step was not changed. A procedure identical to the one described above (substeps 1-3) was then used to obtain $\mathbf{U}^{n+2}$ and C^{n+2}.

The moving boundary scheme has been described elsewhere (18). Briefly, at each time step of boundary movement, the normal unit vector and the concentration gradient on the boundary points were computed. Equation [17] was then used to calculate the velocity of the boundary along the normal direction. The new location of the boundary was then found. Calculations were performed on a CRAY Y-MP supercomputer. The CPU time required for one time step was, on the average, 3s. The time step size depended on the system parameters (*e.g.*, Ra), and was controlled adaptively during the shape evolution calculation. The time step size was in the range 10^{-3} to 10^{-1}.

Forced-convection system.—In the case of forced convection there is no need to use infinite elements since the concentration boundary layer is always confined near the wall, for the parameter values used. In this case, the position of boundaries Γ_2, Γ_3, and Γ_4 (see Fig. 2) was chosen at $X = -5$, $Y = 4$, and $X = 5$, respectively. Numerical experiments revealed that the results were not affected by positioning boundaries Γ_2, Γ_3, and Γ_4 further away from the cavity mouth. As the cavity became deeper during etching, new elements were added to maintain a fine spatial discretization within the cavity. The fluid velocity and concentration fields were obtained by using the penalty function formulation and the SU/PG method. The moving boundary scheme was the same as before (18). Computations were performed on a CRAY Y-MP supercomputer.

Results and Discussion

Results are first presented for the forced convection system followed by results for the natural convection system. Velocity vector plots and iso-concentration contour plots are used to depict the flow and concentration fields, respectively. The velocity scale in all vector plots is noted in the corresponding figure caption. For example, a scale of 1.1×10^4 implies that the magnitude of the velocity of a vector with length equal to the cavity half mouthwidth is equal to 1.1×10^4 dimensionless units (defined by Eq. [6]). All results shown below were obtained for a value of the Schmidt number Sc = 10^3, which is typical for aqueous solutions, and for a value of B = 100. The instantaneous etching rate of a point on the active surface is proportional to the local Sherwood number (Eq. [17] and [19]). All results are in terms of dimensionless quantities.

Figure 4a shows the shape evolution of a cavity under the influence of forced convection for a value of Pe = 10^3 (Re = 1). Other conditions were B = 100, and initial aspect ratio of the cavity (depth:width) 1:2 (only part of the mask thickness is shown in Fig. 4a). Figure 4b shows the corresponding Sherwood number as a function of position (X-coordinate) along the active surface, for different times during etching. In essence, Fig. 4b shows the instantaneous etching rate distribution along the active surface. The etching rate distribution along the active surface is asymmetric, the rate being higher to the right of the cavity centerline (X = 0), especially at early times. This leads to asymmetric cavity wall profiles. The asymmetry is associated with a clockwise eddy which fills a large fraction of the cavity volume (fluid was entering the cavity region from the left). The etching rate is enhanced at the location where the eddy first encounters the cavity bottom, *i.e.*, to the right of the centerline. Secondary eddies are formed in the undercut regions, but their intensity is much reduced compared to the main eddy. The end points of each curve in Fig. 4b correspond to the points where the mask and the active surface meet. Hence, these points provide an idea of the instantaneous rate of mask undercut. The rate of undercut of the right mask is higher at all times due to the clockwise eddy referred to above. The etching rate distribution is highly nonuniform at early times, the rate of vertical etching being much higher than the rate of mask undercut. This enhances the etch anisotropy. However, the distribution becomes nearly uniform at later times when the cavity becomes deep, and the effect of convection is diminished. Therefore, the etch factor decreases with time. Furthermore, the spatially-average etching rate decreases sharply with time as the cavity deepens.

Figure 5a shows the shape evolution of a cavity under conditions identical to those in Fig. 4a, except that the initial cavity aspect ratio was 1:1. The corresponding local Sherwood number distribution is shown in Fig. 5b. Since the cavity is deeper, the etching rate is reduced compared to Fig. 4. The reduction in etching rate, and the resulting longer etch time lead to a higher mask undercut, reducing the etch factor. As before, the etching rate distribution is very nonuniform at early times, turning to nearly uniform at later times. A characteristic of this case is the higher etching rate to the left of the cavity centerline observed at late times (*e.g.*, T = 480 in Fig. 5b). This phenomenon is more pronounced for higher values of the Pe number as discussed below.

Figure 6a shows the shape evolution of a cavity under conditions identical to those of Fig. 5, except that Pe = 10^4 (Re = 10). The corresponding Sherwood number distribution is shown in Fig. 6b. The etching rate is higher than in Fig. 5 owing to the increased level of convection. In addi-

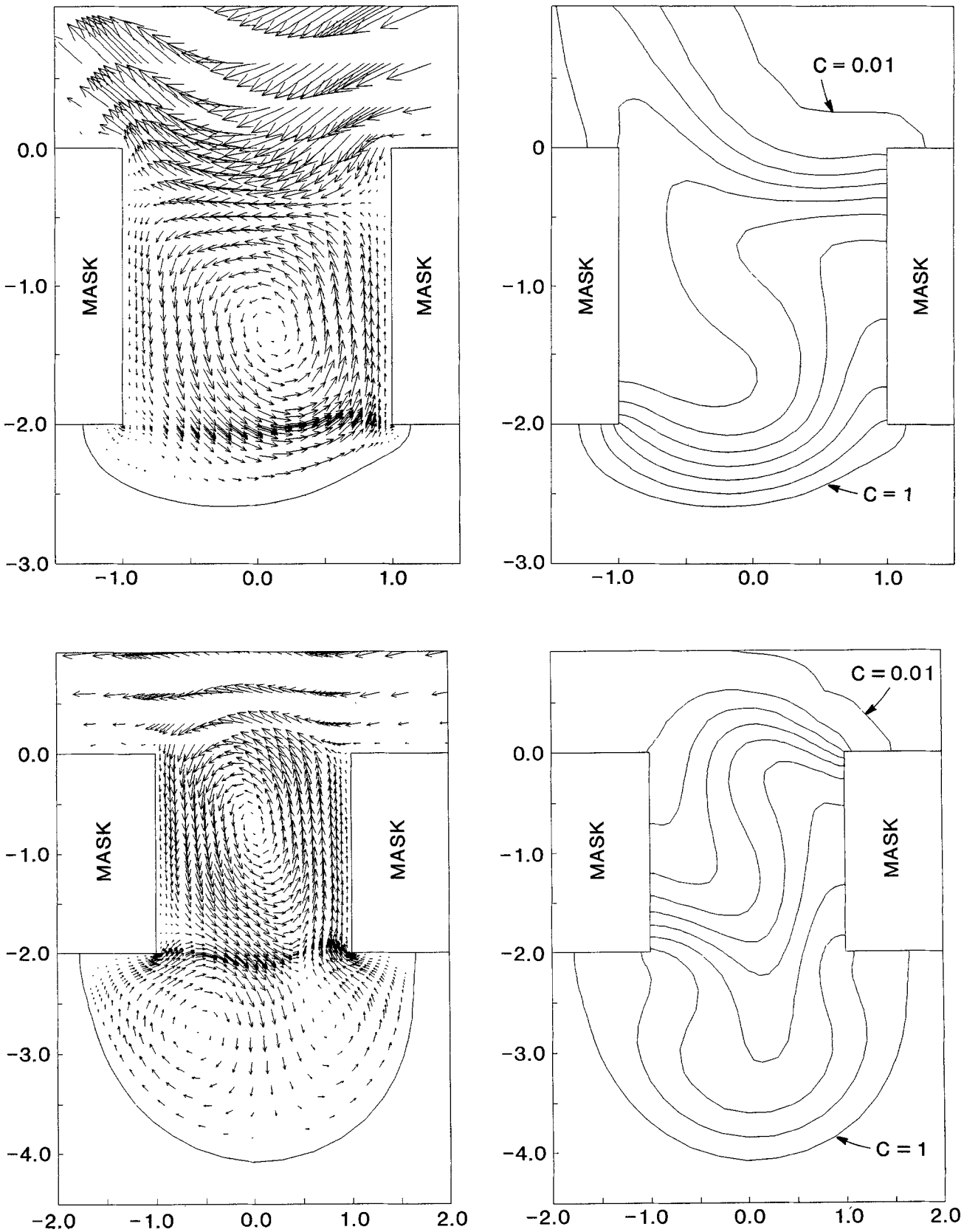

Fig. 10. (a, top left) Velocity vector plot in the cavity corresponding to time $T = 55.6$ of Fig. 9. (b, top right) Concentration contour plot in the cavity corresponding to (a). (c, bottom left) Velocity vector plot in the cavity corresponding to time $T = 290$ of Fig. 9. (d, bottom right) Concentration contour plot in the cavity corresponding to (c). Linear interpolation applies for the contours between $C = 0.01$ and $C = 1$ (wall of cavity). Velocity scale for (a) and (c) is 50.

tion, as in the previous cases, the spatially-averaged etching rate decreases dramatically with time as the cavity deepens. The cavity wall profiles are asymmetric. At early times, etching is faster to the right of the centerline. However, at later times etching is faster to the left of the centerline. In order to explain the observed phenomena, one needs to consider the hydrodynamic flow patterns within the cavity as the cavity deepens during etching. At early times, most of the cavity volume is filled by a single main eddy which rotates clockwise. The etching rate is higher to the right of the centerline where this eddy first encounters the cavity bottom (see also Fig. 4). At later times, the cavity

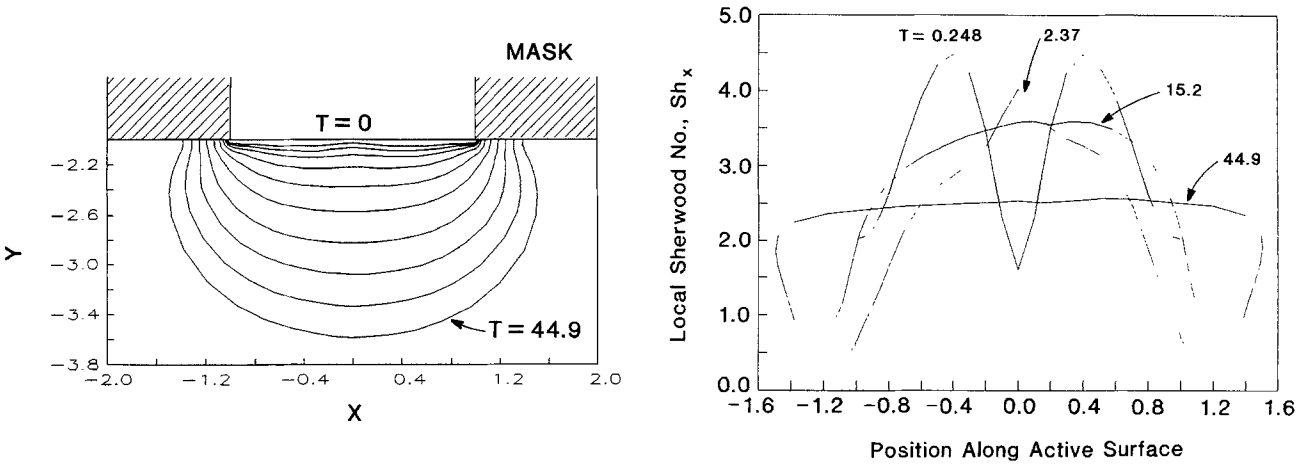

Fig. 11. (a, left) Shape evolution of a cavity with initial aspect ratio of 1:1 under natural convection. Other conditions were Ra = 10^4 and B = 100. Cavity wall profiles are shown for dimensionless times T = 0, 1.37, 2.37, 3.71, 6.01, 9.84, 15.2, 22.2, 29.5, 37.0, and 44.9. (b, right) Local Sherwood number (instantaneous etching rate) distribution along the active surface at different times during etching. Conditions were as in (a).

becomes deep enough for a secondary eddy to form underneath the first. The velocity vector plot of Fig. 7a shows the hydrodynamic pattern within the cavity at time T = 143. The main clockwise eddy driven by the external flow is clearly seen, and it is much weaker than the external flow. The secondary eddy cannot be resolved on the velocity scale used in Fig. 7a. The expanded scale of Fig. 7b shows the secondary eddy rotating counterclockwise, underneath the main eddy. It is because of this counterclockwise motion that the etching rate and the rate of mask undercut are higher to the left of the centerline, once the secondary eddy forms. One further observes that the secondary eddy is much weaker than the main one. Tertiary eddies are also formed in the undercut regions, but these eddies are extremely weak. The concentration contour plot corresponding to the cavity at T = 143 is shown in Fig. 8. The "contaminated" solution is essentially trapped within the deep cavity. The contours deep in the cavity are nearly parallel to the active surface. This implies that the effect of convection is weak there, and transport by diffusion plays a dominant role. The spacing between the contours is an indication of the local mass-transfer rate (and etching rate). One observes that the etching rate is higher to the left of the centerline for the reason explained above.

It is apparent from the aforementioned results that forced convection is not effective for rinsing the reaction products out of deep cavities. Once the cavity becomes deep enough for recirculating eddies to form, communication between the external flow and the inside of the cavity becomes weak. This results in long etching times and high mask undercut. Natural convection can restore the lost communication between the external and the internal of the cavity.

Figure 9a illustrates the shape evolution of a cavity under the influence of natural convection, for Ra = 10^3. The initial aspect ratio of the cavity was 1:1, and B = 100. The corresponding Sherwood number distribution is shown in Fig. 9b. There are two distinct differences between the natural convection case and the corresponding forced convection case (Fig. 5 and 6). First, the decrease in the spatially-average etching rate with time is much slower in the case of natural convection, *i.e.*, the etching rate remains relatively high even when the cavity becomes deep. Second, the etching rate in the vertical direction (around X = 0), remains substantially higher than the rate of mask undercut throughout etching, even when the cavity becomes deep (compare Fig. 9b to Fig. 5b and 6b). This implies that high etch factors can be obtained, even when etching of high aspect ratio cavities is desired. The cavity wall profiles are asymmetric, especially at early times. This can be explained by examining the fluid flow patterns within the cavity.

Figure 10a shows the velocity vector plot in the cavity corresponding to time T = 55.6 of Fig. 9a. A single natural convection cell exists, rotating counterclockwise. The etching rate is higher at the location where the recirculating fluid first encounters the cavity bottom, *i.e.*, to the left of the cavity centerline. The corresponding concentration contour plot is shown in Fig. 10b. The contours are distorted according to the hydrodynamic flow patterns. Figure 10c depicts the velocity vector plot in the cavity corresponding to time T = 290 of Fig. 9a. When compared to Fig. 10a, one observes additional cells formed deeper in the cavity. The fluid velocity remains at a relatively high value throughout the core of the cavity. This is in contrast to the forced convection case (Fig. 7a). The concentration contour plot corresponding to Fig. 10c is shown in Fig. 10d. The contaminated solution is rinsed out of the cavity bottom more effectively, as compared to the forced convection case (Fig. 8).

The beneficial effects of natural convection are made more apparent when the intensity of the convection increases. Figure 11a shows the shape evolution of a cavity under conditions identical to those of Fig. 10, except that Ra = 10^4. The corresponding Sherwood number distribution is shown in Fig. 11b. As expected, the etching rate is much higher as compared to Fig. 10. In fact, it takes four times shorter to etch a depth of 1.6 dimensionless units, when compared to Fig. 10 (one dimensionless unit corresponds to a length equal to half the cavity mouthwidth). The cavity wall profiles are W-shaped at early times. This corresponds to an etching rate distribution showing a minimum around X = 0 at early times (T = 0.248, Fig. 11b). At later times (T = 2.37), the rate peaks around the center, leading to disappearance of the W-shaped profile. At even later times, the rate is rather uniform along the cavity walls except for a sharp drop of the rate in the mask undercut regions. This implies that a high etch factor is maintained, even when the cavity becomes deep. Another interesting phenomenon observed in Fig. 11a is the cavity width being largest at a location other than where the active surface meets the mask. This is clearly seen in the contour corresponding to T = 44.9 in Fig. 11a. A better understanding of the above phenomena can be gained by having a closer look at the fluid flow and product concentration patterns within the cavity.

Figure 12a shows the velocity vector plot corresponding to the cavity at time T = 0.248, etching under the conditions of Fig. 11. Although the natural convection patterns are well developed, the cavity wall has not receded appreciably at this early time. Two symmetrical natural convection cells provide for effective communication, bringing fresh solution inside the cavity and washing the dissolution products away. The same features are seen in the corresponding concentration contour plot (Fig. 12b). One observes the formation of a "plume" along the axis of symmetry, by which denser solution flows out of the cavity causing fresh solution to flow into the cavity. The etch-

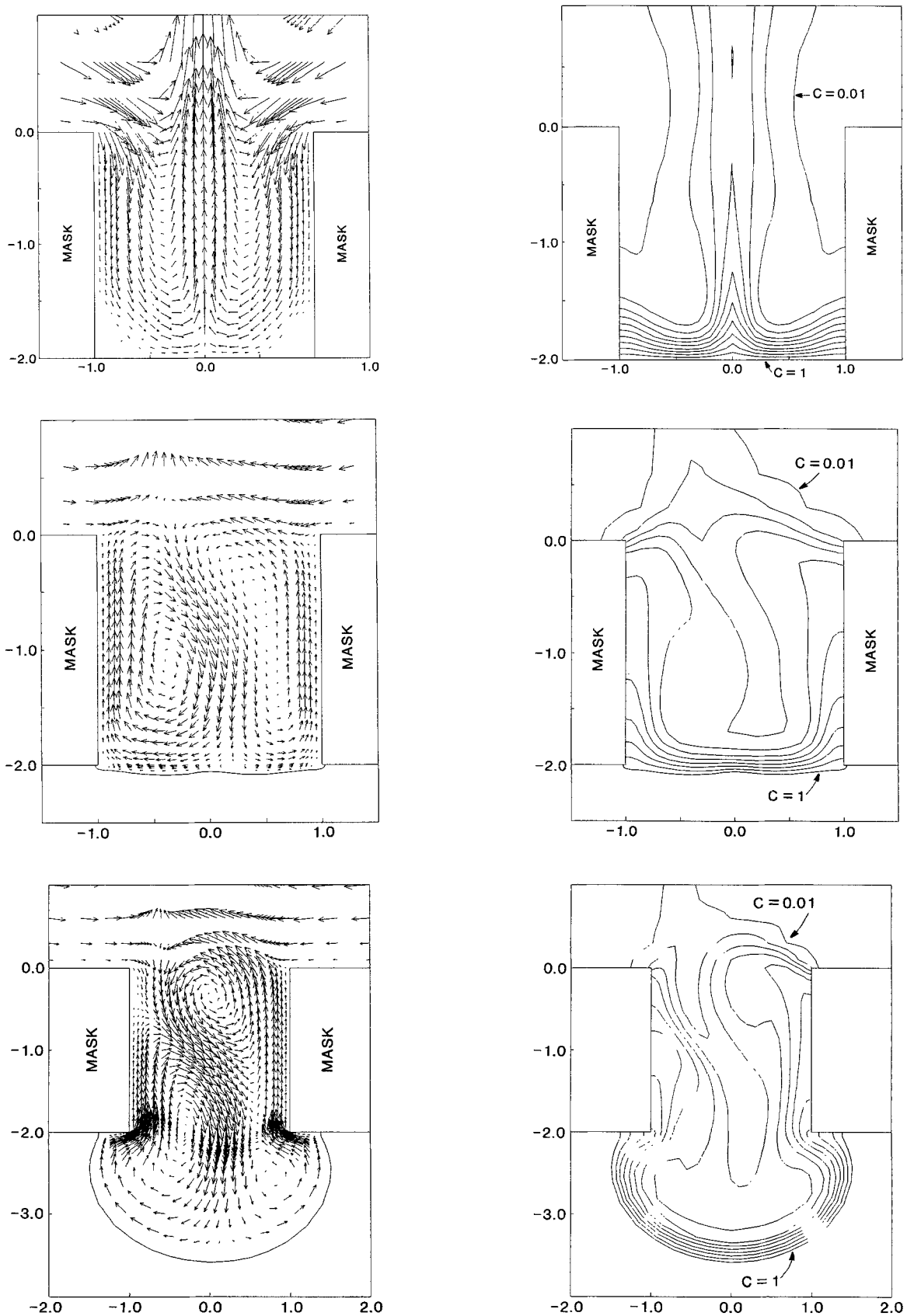

Fig. 12. (a, top left) Velocity vector plot in the cavity corresponding to time $T = 0.248$ of Fig. 11. (b, top right) Concentration contour plot in the cavity corresponding to (a). (c, middle left) Velocity vector plot in the cavity corresponding to time $T = 2.37$ of Fig. 11. (d, middle right) Concentration contour plot in the cavity corresponding to (c). (e, bottom left) Velocity vector plot in the cavity corresponding to time $T = 44.9$ of Fig. 11. (f, bottom right) Concentration contour plot in the cavity corresponding to (e). Linear interpolation applies for the contours between $C = 0.01$ and $C = 1$ (wall of cavity). Velocity scale for (a), (c), and (e) is 300.

ing rate has a minimum around $X = 0$, since the flow is directed away from the surface in that region. This minimum in the etching rate distribution results in the W-shaped wall profiles of the cavity at early times. Figures 12c and d depict the situation at time $T = 2.37$. The fluid velocity and concentration profiles are no longer symmetric. Symmetry breaking and oscillatory flows were found to occur in cavities of fixed shape (13). Similar symmetry breaking has

also been reported by Weber *et al.* (31), in two-dimensional vertical vapor-phase epitaxy reactors. The authors presented a bifurcation diagram showing the transition between symmetric and asymmetric flows. Despite the asymmetry of the system shown in Fig. 12c, there are still two main natural convection cells, except that the direction of rotation of the cells has reversed (compared to Fig. 12a). This reversal in flow direction enhances the reaction rate around $X = 0$ (see also Fig. 11b, $T = 2.37$). This in turn leads to the gradual disappearance of the W-shaped cavity wall profiles. The flow reversal has a big advantage, since the reaction rate along the vertical direction is enhanced, and the etch anisotropy is therefore improved. The situation inside the cavity at time $T = 44.9$ is illustrated in Fig. 12e and f. The cellular flow patterns within the cavity are indeed very complex. However, the essential (and beneficial) features remain. For example, the fluid motion is strong even deep inside the cavity, leading to relatively high etching rate. Further, fresh fluid first encounters the cavity bottom around the centerline, and then flows along the cavity active walls. The resulting "boundary layer" is thickest in the undercut regions, which in turn results in lower rate of undercut and enhanced anisotropy.

Results on etching rate are summarized in Fig. 13, for the cavity with an initial aspect ratio of 1:1. The dimensionless etching rate was found by dividing the cavity depth by the elapsed time, *i.e.*, this is a cumulative etching rate as one would measure after etching for time T. Etching rate results for pure diffusion (no fluid flow) have also been included in Fig. 13 as curve I. As expected, the etching rate increases with Pe for the case of forced convection (compare curves II and III), and with Ra for the case of natural convection (compare curves IV and V). However, there exists a striking difference between forced and natural convection. The etching rate achieved by forced convection decreases sharply with time as the cavity becomes deeper. In contrast, the etching rate achieved by natural convection remains relatively constant with time, even when the cavity becomes deeper. This has important implications for etching of deep cavities.

Figure 14 summarizes the etch factor (EF) results for the cavity with an initial aspect ratio of 1:1. As in Fig. 13, dimensionless time refers to the elapsed time T. The EF achieved by pure diffusion remains essentially constant, independent of etching time. Forced convection (curves II and III) offers high EF initially, but the EF degrades dramatically as time elapses and the cavity becomes deeper. In fact, forced convection may result in worst EF compared to pure diffusion, as seen in Fig. 14 for Pe = 10^3 and

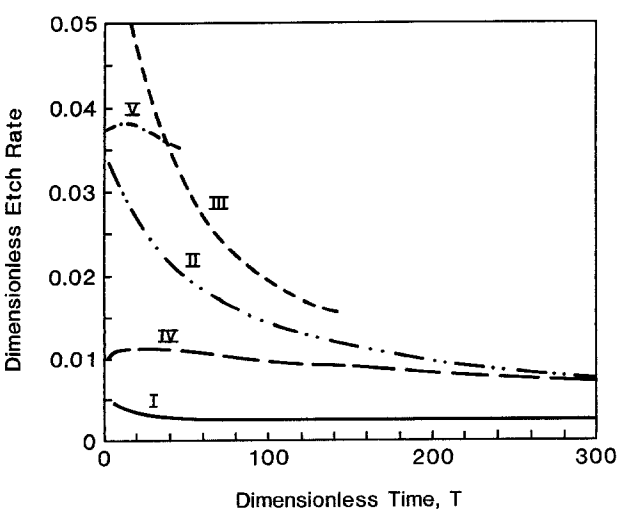

Fig. 13. Dimensionless etching rate as a function of the cumulative time for cavities etching under the conditions of pure diffusion with $B = 100$ (curve I), forced convection corresponding to Fig. 5 (curve II), forced convection corresponding to Fig. 6 (curve III), natural convection corresponding to Fig. 9 (curve IV), and natural convection corresponding to Fig. 11 (curve V).

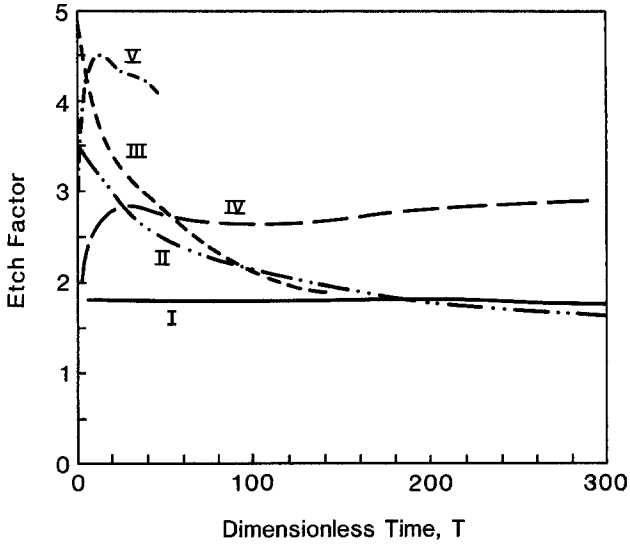

Fig. 14. Etch factor as a function of the cumulative time for cavities etching under the condition of pure diffusion with $B = 100$ (curve I), forced convection corresponding to Fig. 5 (curve II), forced convection corresponding to Fig. 6 (curve III), natural convection corresponding to Fig. 9 (curve IV), and natural convection corresponding to Fig. 11 (curve V).

$T > 180$. In the case of natural convection, and for Ra = 10^3, the etch factor initially increases with time, passes through a shallow minimum and then increases slowly with time (curve IV). For Ra = 10^4, the etch factor increases sharply with time at early times. The reason for this can be explained as follows. At early times, the convective motion is such that fresh solution flows into the cavity along the mask walls and contacts the mask undercut regions first (see Fig. 12a). Hence the rate of mask undercut is relatively higher and the EF is lower. At later times the flow direction reverses (Fig. 12c), and the rate of mask undercut drops while the vertical etching rate is still high (Fig. 11b, $T = 2.37$). Hence the etch factor increases sharply. At still later times, when large recirculating cells form in the undercut regions (Fig. 12e), the rate of mask undercut increases again (compare curves for $T = 2.37$ and $T = 44.9$ of Fig. 11b), resulting in diminishing etch factor.

Summary and Conclusions

The effect of forced and natural convection on the shape evolution of cavities during wet chemical etching was investigated. Etching was assumed to be limited by the removal of dissolution products from the vicinity of the reactive surface. Initial cavity aspect ratios (depth:width) of 1:1 and 1:2 were examined, with emphasis on the 1:1 cavity. Values of Pe number and of Rayleigh number of up to 10^4 were studied. Finite element methods were employed to solve for the fluid velocity and the concentration distribution in domains of irregular shape resulting by etching. The method of mapped infinite elements was used to model the unbounded domain in the case of natural convection. A moving boundary scheme was developed to track the shape evolution of the cavity under diverse etching conditions. The results apply equally well to the case of etching being limited by diffusion of etchant to the reactive surface.

Forced convection was very ineffective for rinsing the dissolution products out of the cavity for the cases studied. This was due to slow recirculating eddies within the cavity preventing effective communication between the external flow and the inside of the cavity. The etching rate decreased sharply with time as the cavity became deeper. At the same time, the etching rate distribution along the active surface became nearly uniform, degrading etch anisotropy. At early times during etching, when a single main eddy occupied most of the cavity volume, the etching rate was higher to the right of the cavity centerline, due to the clockwise motion of that eddy (the external flow direction was from the left). At later times when the cavity became

deep enough for a second counterclockwise eddy to form underneath the first, the etching rate was higher to the left of the centerline. Nevertheless, the fluid motion was very weak deeper in the cavity, and transport by diffusion played a major role. For long enough times, the etch factor achieved by forced convection was lower than that achieved by pure diffusion. This underscores the ineffectiveness of forced convection for deep anisotropic etching. In this work emphasis was placed on etching of high aspect ratio (deep) cavities. For shallow cavities, forced convection is very effective for enhancing the etch rate and improving the etch factor.

Natural convection was effective for rinsing the dissolution products out of the cavity for the high aspect ratio (deep) cavities. Both the etching rate and the etch factor remained at relatively high values throughout etching, even at later times when the cavity became deeper. This was attributed to plumes of denser solution flowing out of the cavity, causing fresh solution to flow into the cavity, thereby providing effective communication between the outside and the inside of the cavity.

The cavity wall profiles and the corresponding flow and concentration fields showed some interesting features for the case of $Ra = 10^4$. The wall profiles were W-shaped at early times. This was due to two symmetrical natural convection cells formed within the cavity, such that the etching rate had a local minimum around the cavity center ($X = 0$). At later times, the flow direction of the cells reversed and symmetry breaking was observed. The etch rate was then highest around the cavity center, causing the W-shaped profile to disappear. The etch factor increased sharply with time at early times, passed through a maximum and then decreased rather slowly with time at later times. It appears that an etch factor greater than 2.5 is very difficult, if at all possible, to achieve using forced convection to etch a cavity to a final aspect ratio greater than 2:1. In contrast, an etch factor of greater than four may be achieved using natural convection enhanced etching.

The system examined in the present work is only a simplification of a real etching system. For example, solution and/or surface chemistry may play a role, and any gas evolution would alter the hydrodynamic patterns inside the cavity. Gas evolution is expected to enhance the etch rate in deep cavities. In fact, for such cavities, gas evolution may have the same beneficial effects as natural convection. Despite the simplifications, the model provided valuable insight on the effect of forced convection and especially of natural convection on the shape evolution of deep cavities.

There is a wide variety of processes involving transport with chemical reaction in a complex geometry which is continually changing as a result of the process. Examples include chemical and electrochemical etching (4), electrodeposition through masks (19), and localized corrosion (11). Powerful mathematical techniques based on the finite element method, and the availability of supercomputers have made the numerical simulation of such processes feasible. The simulation tools can be very useful for gaining a better understanding of the intricate nature of the process, for the optimization of existing processes, and for the development of new ones.

Acknowledgments

We are grateful to the Pittsburgh Supercomputer Center (supported by NSF) for a supercomputer-time grant. Supercomputer time for the initial stages of this work was provided by Cray Research Incorporated (Mr. David Dealy, grant minor).

Manuscript submitted April 10, 1990; revised manuscript received Sept. 10, 1990.

The University of Houston assisted in meeting the publication costs of this article.

LIST OF SYMBOLS

A	aspect ratio, $h/2L$
B	parameter, Eq. [18]
c	species concentration, mol/m^3
c_∞	far-field species concentration, mol/m^3
c_{sat}	species concentration at saturation, mol/m^3
C	dimensionless species concentration, $(c - c_\infty)/(c_{sat} - c_\infty)$
D	diffusivity, m^2/s
h	initial cavity height, m
$\mathbf{j}$	unit vector in the y direction
k_x	local mass-transfer coefficient, m/s
M_s	molecular weight of solid, kg/mole
p	pressure, Pa
P	dimensionless pressure, $P = (p - \rho_\infty \alpha y)L^2/(\mu D)$
Pe	Peclet number, Pe = Re Sc
Ra	Rayleigh number, $Ra = \alpha\beta\,(c_{sat} - c_\infty)L^3/(\nu D)$
Re	Reynolds number, $Re = u_c L/\nu$
Sc	Schmidt number, $Sc = \nu/D$
Sh_x	local Sherwood number, $Sh_x = k_x L/D$
t	time, s
T	dimensionless time, $T = tD/L^2$
$\mathbf{u}$	fluid velocity vector
$\mathbf{U}$	dimensionless fluid velocity vector, $\mathbf{U} = L\mathbf{u}/D$
u_c	fluid velocity at center of cavity mouth, m/s
U_x	x-component of dimensionless fluid velocity
U_y	y-component of dimensionless fluid velocity
v_n	velocity of moving boundary, Eq. [16], m/s
V_n	dimensionless velocity of moving boundary, Eq. [17]
x	horizontal spatial coordinate, m
X	dimensionless horizontal spatial coordinate, x/L
y	vertical spatial coordinate, m
Y	dimensionless vertical spatial coordinate, y/L

Greek

α	gravitational acceleration, m/s^2
β	coefficient of volume expansion, m^3/mole
μ	viscosity, kg/m-s
ν	kinematic viscosity, m^2/s
ρ	density, kg/m^3
ρ_∞	far-field density, kg/m^3
ρ_s	density of solid, kg/m^3
σ	parameter, Eq. [18], m^5/mol-s
Σ	dimensionless shear rate, Eq. [21]

REFERENCES

1. "Thin Film Processes," J. L. Vossen and W. Kern, Editors, Academic Press, Inc., New York (1978).
2. S. K. Ghandhi, "VLSI Fabrication Principles," John Wiley & Sons, Inc., New York (1983).
3. R. M. Lum, F. W. Ostermayer, Jr., P. A. Kohl, A. M. Glass, and A. A. Ballman, *Appl. Phys. Lett.*, **47,** 269 (1985).
4. M. Datta and L. T. Romankiw, *This Journal*, **136,** 285C (1989).
5. G. Kaminsky, *J. Vac. Sci. Technol.*, **B3,** 1015 (1985).
6. D. W. Shaw, *This Journal*, **128,** 874 (1981); *J. Cryst. Growth*, **47,** 509 (1979).
7. D. M. Allen, D. F. Horne, and G. W. W. Stevens, *J. Photog. Sci.*, **27,** 181 (1979).
8. R. Alkire and L. Deligianni, *This Journal*, **135,** 1093 (1988).
9. D. V. Podlesnik, H. H. Gilgen, A. E. Willner, and R. M. Osgood, Jr., *J. Opt. Soc. Am. B*, **3,** 775 (1986).
10. H. K. Kuiken and R. P. Tijburg, *This Journal*, **130,** 1722 (1983).
11. R. C. Alkire, D. B. Reiser, and R. L. Sani, *ibid.*, **131,** 2795 (1984).
12. H. K. Kuiken, *J. Eng. Math.*, **12,** 129 (1978).
13. C. B. Shin and D. J. Economou, *Int. J. Heat & Mass Trans.*, **33,** 2191 (1990).
14. C. Vuik and C. Cuvelier, *J. Comput. Physics*, **59,** 247 (1985).
15. H. K. Kuiken, *Proc. R. Soc. London, Ser. A*, **396,** 95 (1984).
16. H. K. Kuiken, *ibid.*, **392,** 199 (1984).
17. H. K. Kuiken, J. J. Kelly, and P. H. L. Notten, *This Journal*, **133,** 1217 (1986).
18. C. B. Shin and D. J. Economou, *ibid.*, **136,** 1997 (1989).
19. E. C. Hume, W. M. Deen, and R. A. Brown, *ibid.*, **131,** 1251 (1984).
20. P. Bettess, *Int. J. Num. Meth. Engng.*, **15,** 1613 (1980).
21. G. Beer and J. L. Meek, *ibid.*, **17,** 43 (1981).
22. P. P. Lynn and H. A. Hadid, *ibid.*, **17,** 347 (1981).
23. O. C. Zienkiewicz, C. Emson, and P. Bettess, *ibid.*, **19,** 393 (1983).
24. J. M. M. C. Marques and D. R. J. Owen, *Comput. Structures*, **18,** 739 (1984).
25. T. J. R. Hughes, W. K. Liu, and A. Brooks, *J. Comput.*

Phys., **30,** 1 (1979).
26. A. N. Brooks and T. J. R. Hughes, *Comput. Meth. Appl. Mech. Engng.*, **32,** 199 (1982).
27. T. J. R. Hughes, K. S. Pister, and R. L. Taylor, *ibid.*, **17/18,** 159 (1979).
28. H. E. Bailey, *Phys. Fluids*, **12,** 2292 (1969).
29. J. H. Argyris and J. St. Doltsinis, *Comput. Meth. Appl. Mech. Engng.*, **25,** 195 (1981).
30. J. H. Argyris, J. St. Doltsinis, P. M. Pimenta, and H. Wustenberg, *ibid.*, **45,** 3 (1984).
31. C. Weber, C. van Opdorp, and M. de Keijser, *J. Appl. Phys.*, **67,** 2109 (1990).

Effect of Heat-Treatment on the Magnetic and Structural Properties of Perpendicular Magnetic Anisotropy CoNiReP Films Produced by Electroless Deposition

Tetsuya Osaka,* Takayuki Homma, and Katsumi Inoue**

Department of Applied Chemistry, Waseda University, Shinjuku-ku, Tokyo 169, Japan

ABSTRACT

The effect of heat-treatment on the magnetic and structural properties of electroless-plated CoNiReP films with various compositions were studied to determine their microstructure in the as-deposited conditions, as well as to estimate their thermal stability. Due to the difference in compositions, magnetic properties of the films were found to behave differently with heat-treatment. The films with high crystallinity showed larger changes in magnetic properties. The $Co_{32}Ni_{55}Re_6P_7$ film with the largest perpendicular magnetic anisotropy kept its positive anisotropy energy with treatment up to 500°C. The <002>-oriented hcp structure of this film was also maintained with treatment up to 500°C. However, heat-treatment at 600°C altered the crystal structure of the films from the <002> oriented hexagonal close-packed structure to face-centered cubic without preferred crystal orientation, causing a sharp change in the magnetic properties of the films. Since the formation of Ni_3P compound and fcc regions was detected in the film with treatment higher than 500°C, it was assumed that in the as-deposited films the <002>-oriented hcp crystallites with high crystallinity segregate in the amorphous NiP phase.

The authors have developed electroless-plated CoNiReP films for perpendicular magnetic recording and have investigated their characteristics successively (1-8). In our previous study (9), we reported that the magnetic and structural properties of the films change widely with changes in composition, and that the $Co_{32}Ni_{55}Re_6P_7$ film shows the largest perpendicular magnetic anisotropy. Even though the face-centered cubic (fcc) structure is expected for a film with such a Ni-rich composition (10), the film mainly consists of <002>-oriented hexagonal close-packed (hcp) structure, which can be maintained due to its segregated microstructure (11).

In this study, the effect of heat-treatment on magnetic and structural properties of electroless-plated CoNiReP films was investigated to help clarify the microstructure of the as-deposited films as well as to evaluate their thermal stability.

Experimental

Table I shows the basic composition and operating conditions of the electroless-plated bath applied to this study. Films 2 μm thick were plated from this bath onto polished Cu substrates. To initiate the deposition, surfaces of the substrates were activated and accelerated immediately before plating (12). Film composition was changed by varying the cobalt sulfate concentration in the bath and was determined using an inductively coupled argon plasma atomic emission spectrophotometer (ICP; ICAP-575 Mark II, Nippon, Jarrel and Ash, Limited). The heat-treatment of the specimen films was carried out at 2×10^{-3} Pa with a constant heating rate of 10°C min^{-1} from room temperature, after which the specimens were maintained for 60 min at temperatures up to 700°C. Magnetic properties were measured with a vibrating sample magnetometer (VSM; BHV-30, Riken Denshi, Limited) and with a torque magnetometer (TM; TM-2050HGC, Tamakawa Seisakusyo, Limited). Structural properties were studied with x-ray diffractometry (XRD; Rad IIA, Rigaku Denki, Limited, Fe Kα), scanning electron microscopy (SEM; JSM-T20, JEOL, Limited), transmission electron microscopy, transmission high-energy electron diffraction, and reflection high-energy electron diffraction (TEM, THEED, and RHEED; HU-12A, Hitachi, Limited, 100 kV). All measurements were carried out at room temperature after the heat-treatment.

* Electrochemical Society Active Member.
** Electrochemical Society Student Member.

Results and Discussion

In this study, four typical compositions (A, B, C, and D shown in Table II) were selected from our previous research (9). The representative properties of the as-deposited films are shown in Table II. Film A of low cobalt content with low XRD peak intensity of hcp (002) plane, $I_{(002)}$, shows low crystallinity. Film B with higher peak intensity of $I_{(002)}$ shows high crystallinity and keeps the highest anisotropy energy, *Ku*, namely, the film has the largest perpendicular magnetic anisotropy. Film C with the highest peak intensity of $I_{(002)}$ shows the highest crystallinity, but has a negative *Ku* value. Film *D* with the lowest crystallinity shows in-plane anisotropy.

The anisotropy energy, *Ku*, of the films is plotted against the heat-treatment temperature in Fig. 1. Film B with the largest perpendicular anisotropy keeps a positive *Ku* for heat-treatment up to 500°C. It sharply decreases at around 500°C and turns negative for treatment higher than 600°C. The *Ku* value of film A stays around zero for heat-treatment up to 700°C.

Table I. Basic bath composition and operating conditions for electroless CoNiReP films

Chemicals	Concentration (mol dm^{-3})
$NaH_2PO_2\ H_2O$	0.20
$(NH_4)_2SO_4$	0.50
$CH_2\ (COONa)_2\ H_2O$	0.75
$C_2H_2\ (OH)_2\ (COONa)_2\ 2H_2O$	0.20
$CH\ (OH)\ (COOH)_2$	0.05
$CoSO_4\ 7H_2O$	0.00-0.20
$NiSO_4\ 6H_2O$	0.08
NH_4ReO_4	0.003
Bath temperature	80°C
pH (adjusted using NH_4OH)	8.7